JGR Solid Earth

RESEARCH ARTICLE
10.1029/2025JB031560

Super-Shear and Generalized Rayleigh Rupture of the 2023 Turkey Earthquake Doublet Influenced by Fault Material Contrast

Hongyu Zeng[1,2], Zhangfeng Ma[1], Chenglong Li[2], Xinzhong Yin[1], Yu Jiang[1], Yukuan Chen[1], Ares Rosakis[3], Ozgun Konca[4], and Shengji Wei[1,2,5]

[1]Earth Observatory of Singapore, Nanyang Technological University, Singapore, Singapore, [2]Asian School of the Environment, Nanyang Technological University, Singapore, Singapore, [3]Aerospace (GALCIT) and Mechanical Engineering, California Institute of Technology, Pasadena, CA, USA, [4]Bogazici University Kandilli Observatory and Research Institute, Department of Geophysics, Istanbul, Turkey, [5]Key Laboratory of Deep Petroleum Intelligent Exploration and Development, Institute of Geology and Geophysics, Chinese Academy of Sciences, Beijing, China

Abstract Rupture speed is a crucial parameter of earthquake dynamics and influencing associated seismic hazards. Accurately resolving the rupture evolution of large earthquakes is essential for identifying factors governing earthquake physics. In this study, we investigate the kinematic rupture processes of the 2023 Mw7.8 and Mw7.7 eastern Turkey earthquake doublet. We integrate various complementary data sets and methods, including 3D surface deformation, teleseismic back-projection, near-fault strong motion waveform analysis, and finite fault inversions, to resolve the rupture details. Our results reveal that the Mw7.8 earthquake predominantly involves an asymmetric bilateral rupture on the main fault, with part of the northeastward rupture reaching super-shear speed (~5.2 km/s), while the southwestward rupture propagates primarily at the generalized Rayleigh speed (~3.4 km/s), a characteristic of an inhomogeneous fault zone separating two dissimilar materials. This directional dependence on rupture speed may be attributed to a material contrast between the softer Anatolian plate and the stiffer Arabian plate, as supported by the fault zone head wave observations and tomography models. In contrast, the Mw7.7 event features a bilateral super-shear rupture, likely due to its occurrence on intraplate faults without substantial material contrast across the fault. This study underscores the importance of incorporating detailed fault zone structures and high-quality near-fault observations into earthquake physics and seismic hazard analysis.

Plain Language Summary An earthquake is produced by the rupture, or rapid dislocation, along a fault. For large earthquakes (e.g., $M > 7.5$), the rupture can propagate for hundreds of kilometers, typically at a speed of several kilometers per second. The intensity of the shaking energy radiated from an earthquake is closely related to the rupture speed, making it a critical parameter for understanding earthquake physics and assessing seismic hazards. In this study, through a holistic analysis of dense seismic and geodetic data sets, we resolve the rupture kinematics of the 2023 Mw7.8 and Mw7.7 eastern Turkey earthquake doublet. We demonstrate that the Mw7.8 event exhibited a bilateral rupture pattern with a northeastward rupture speed exceeding the local shear wave speed, while the southwestward rupture speed closely approached it. This asymmetric pattern aligns well with theoretical predictions and laboratory experiments for faults separating dissimilar materials. Such material contrasts, also evidenced across the fault hosting the Mw7.8 event, appear to have played a significant role during the rupture. Our results underscore the importance of near-fault observations and the integration of multiple data sets and disciplines in the study of earthquake physics.

Key Points:

- Integrated analysis of teleseismic, regional and near-fault data reveals super-shear and generalized Rayleigh rupture speeds in the 2023 Eastern Turkey earthquake doublet
- Fault zone head wave observations indicate a bi-material structure across the Amanos Fault
- The material contrast across the EAF likely played a key role in resulting the asymmetric rupture speed of the Mw7.8 event

Supporting Information:

Supporting Information may be found in the online version of this article.

Correspondence to:

S. Wei,
shjwei@gmail.com

Citation:

Zeng, H., Ma, Z., Li, C., Yin, X., Jiang, Y., Chen, Y., et al. (2025). Super-shear and generalized Rayleigh rupture of the 2023 Turkey earthquake doublet influenced by fault material contrast. *Journal of Geophysical Research: Solid Earth*, *130*, e2025JB031560. https://doi.org/10.1029/2025JB031560

Received 19 MAR 2025
Accepted 17 MAY 2025

Author Contributions:

Conceptualization: Hongyu Zeng, Zhangfeng Ma, Shengji Wei
Data curation: Hongyu Zeng, Zhangfeng Ma, Chenglong Li, Xinzhong Yin, Yu Jiang, Yukuan Chen, Shengji Wei
Formal analysis: Hongyu Zeng, Zhangfeng Ma, Chenglong Li, Yu Jiang, Shengji Wei
Funding acquisition: Shengji Wei
Investigation: Hongyu Zeng, Zhangfeng Ma, Shengji Wei
Methodology: Hongyu Zeng, Zhangfeng Ma, Shengji Wei
Project administration: Shengji Wei
Resources: Shengji Wei
Software: Hongyu Zeng, Zhangfeng Ma, Shengji Wei
Supervision: Shengji Wei
Validation: Hongyu Zeng, Zhangfeng Ma, Ares Rosakis, Shengji Wei

1. Introduction

Earthquake hazards are closely related to the dynamic rupture process that determines the dynamic stress drop and how an earthquake releases destructive seismic energy (Freund, 1979; Hiroo Kanamori & Brodsky, 2004; Lambert et al., 2021; Madariaga, 1983]. While hazard assessments often assume simplified rupture processes (Gerstenberger et al., 2020), actual earthquake ruptures are generally more complex due to unaccounted mechanical (Noda & Lapusta, 2013), geometrical (Hamling et al., 2017), and material (Harris & Day, 1997) heterogeneities within fault zones. Particularly, real earthquakes can exhibit highly variable rupture speeds, ranging from sub-Rayleigh to super-shear (Burridge et al., 1979; Das & Aki, 1977a, 1977b; A. J Rosakis et al., 2007; Xia et al., 2004].

Visualization: Hongyu Zeng, Zhangfeng Ma, Shengji Wei
Writing – original draft: Hongyu Zeng, Zhangfeng Ma, Shengji Wei
Writing – review & editing: Hongyu Zeng, Zhangfeng Ma, Chenglong Li, Xinzhong Yin, Yu Jiang, Yukuan Chen, Ares Rosakis, Ozgun Konca, Shengji Wei

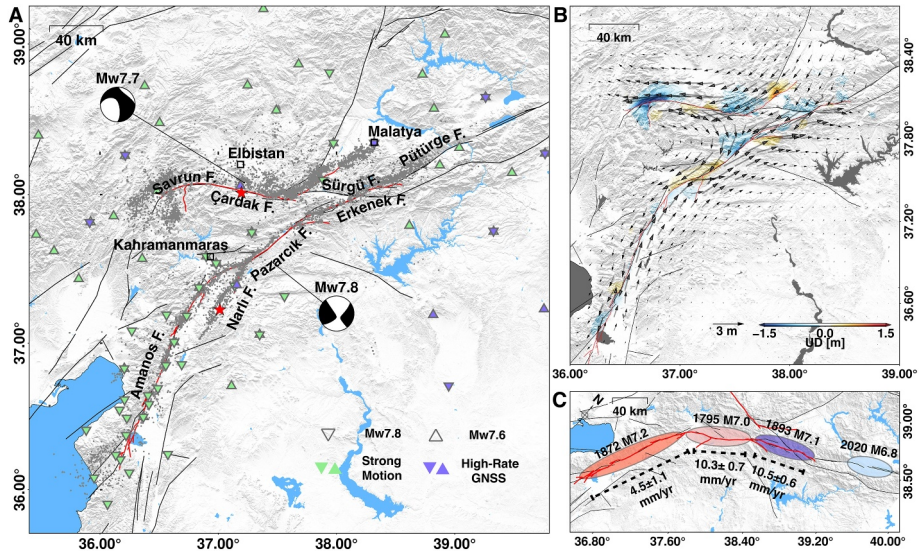

Figure 1. Overview of the East Anatolian Fault (EAF) Zone. (a) Seismotectonic setting of the EAF, illustrating the focal mechanisms of the doublet from the Global Centroid Moment Tensor (GCMT) catalog (Ekstrom et al., 2012) with red stars marking the epicenters (Lomax, 2023). Thin black lines depict active faults (Styron & Pagani, 2020), and red lines indicate the surface fault traces produced by the doublet (Reitman et al., 2023). Gray dots represent aftershocks of the doublet (Ding et al., 2023; Lomax, 2023). (b) 3D static surface deformation resulting from the doublet (Ma, Li, et al., 2024). Color and arrows shows the vertical deformation and horizontal motion, respectively. (c) Distribution of historical large events (ellipses) (Duman & Emre, 2013) and fault parallel strike-slip rates (Aktug et al., 2016) along the left-lateral EAF.

Rupture speed is a key physical parameter governing the dynamic stress field and the partitioning of energy between radiated seismic and fracture energy (Freund, 1979; H. Kanamori et al., 1998). A higher rupture speed indicates a greater amount of energy is radiated as destructive seismic energy (Hiroo Kanamori & Brodsky, 2004; Lambert et al., 2021). Particularly, when a rupture propagates at super-shear speed, a Mach cone develops, along which shear waves from earlier and later ruptures arrive simultaneously, resulting in more destructive ground shaking (Dunham & Bhat, 2008). Therefore, understanding the mechanisms that control rupture speed is crucial for assessing seismic hazards. In this study, we demonstrate that the 2023 Mw7.8&7.7 Turkey earthquake doublet involved complex rupture processes characterized by varying rupture speeds, including sub-Rayleigh, super-shear, and generalized Rayleigh speeds (a characteristic speed of an inhomogeneous fault zone separating two dissimilar materials (Ben-Zion, 2001)). These complex rupture processes carry significant implications for earthquake physics and seismic hazards.

The 2023 Turkey earthquake doublet occurred along the left-lateral East Anatolian Fault (EAF) system, which accommodates the relative motion between the Arabian and Anatolian plates. This system had been seismically quiet for over a century (Nalbant et al., 2002) until 2020 when an Mw6.8 event ruptured the northern EAF (Figures 1a and 1c). On 6 February 2023, a series of powerful earthquakes struck, beginning with an Mw7.8 earthquake that dislocated the south part of the EAF, followed 9 hours later by an Mw7.7 earthquake that ruptured the nearby intraplate faults within the Anatolian plate (Melgar et al., 2023; Reitman et al., 2023). These events resulted in more than 60,000 casualties, left 2.7 million people homeless and caused extensive damage to Turkey and nearby countries. Remote fault mapping (Reitman et al., 2023) and USGS finite fault model analysis (Goldberg et al., 2023) suggests that the Mw7.8 event ruptured faults totaling over 300 km in length, comparable to the 2001 Mw7.9 Kunlunshan and 2002 Mw7.9 Denali intraplate earthquakes. While the Mw7.8 earthquake initiated on the Narlı fault off the main EAF, it primarily ruptured the Erkenek, Pazarcık, and Amanos segments on the EAF, with the fault strike and strike-slip rate changing dramatically from ∼240° to ∼10 mm/yr in the Erkenek and Pazarcık segments to ∼200° and ∼4.5 mm/yr in the Amanos segment (Aktug et al., 2016) (Figures 1a and 1c). The Mw7.7 event has a rupture length of ∼150 km. The majority of the Mw7.7 event rupture is located on the Çardak fault which has an even slower slip rate (∼2.5 mm/yr) (Duman & Emre, 2013). The last major earthquake on this fault likely occurred between 3,215 ± 125 BCE and 825 ± 55 CE (Balkaya et al., 2023). Satellite images have revealed severe destructions along ruptured faults, and extensive off-fault building damages

observed over a large area, including southeast of the Narlı, Erkenek, and Pazarcık segments, northwest of the Pazarcık segment, at the southwest termination of the Anamos segment, and north of the Çardak fault (Voelker et al., 2024; Yu et al., 2024).

The EAF marks a distinct transition in topography, crustal structure, and crustal thickness between the East Anatolian and Arabian plates. For instance, the East Anatolian Plate is, on average, over 1 km higher and features a thicker crust (Ogden & Bastow, 2022) with slower seismic velocities (Delph et al., 2017; Rodgers et al., 2024) and higher seismic attenuation (Zhu et al., 2023) compared to the Arabian plate. Therefore, the EAF effectively acts as a boundary separating two dissimilar materials. Such bi-material fault zones may significantly influence dynamic rupture processes. Theoretical analysis (Adams, 2001; Ranjith & Rice, 2001; Weertman, 1980), numerical modeling (Ben-Zion, 2001; Cochard & Rice, 2000; Harris and Day, 1997), and laboratory experiments (Bhat et al., 2010; A. J. Rosakis et al., 2007; Shlomai & Fineberg, 2016; Xia et al., 2005] support that on faults separating dissimilar materials, bilateral ruptures develop asymmetrically. In the direction where the more compliant material moves toward (defined as the positive direction), strong slip-stress interactions are more likely to result in a pulse-like rupture traveling at the generalized Rayleigh speed if the material contrast is moderate, or at the shear wave speed of the slower material if the material contrast is substantial. Over long distances, the generalized Rayleigh rupture may eventually transition to a super-shear rupture with speed close to the "highest" of the two pressure wave (P-wave) speeds, depending on the material contrast, fault friction, and tectonic stresses (Bhat et al., 2010; A. J. Rosakis et al., 2007; Sammis et al., 2010). Conversely, in the opposite direction (negative direction), super-shear rupture propagation near the "lowest" of the two compressive wave speeds is more likely. The role of this mechanism in the dynamic rupture processes of the 2023 Turkey doublet has not been thoroughly discussed.

The Turkey earthquake doublet was extensively documented through diverse data sets, including dense strong motion stations spanning from near-fault to regional distances, GNSS stations, teleseismic stations, and both optical and SAR satellite imagery. Notably, over 15 strong motion stations are located within 5 km of the Amanos fault trace (Figure 1a). To constrain the slip distribution and kinematic rupture processes of the earthquake doublet, these data sets have been analyzed using various techniques, either individually or in combination (e.g., static and/or kinematic finite fault inversion, multiple point source inversion, back-projection, forward dynamic modeling, and mechanistic analysis of near-fault record signatures) (Abdelmeguid et al., 2023; Barbot et al., 2023; Chen et al., 2024; Delouis et al., 2024; Gabriel et al., 2023; He et al., 2023; Jia et al., 2023; Liu et al., 2023; Mai et al., 2023; Melgar et al., 2023; Okuwaki et al., 2023; A Rosakis et al., 2023; Wang et al., 2023; Xu et al., 2023; Zhang et al., 2023). The two earthquakes are characterized by bilateral ruptures, with the Mw7.8 event featuring ruptures propagating northeast and southwest, and the Mw7.7 event exhibiting east and west propagations.

High-quality and dense geodetic and strong motion data have enabled high-resolution measurements of surface deformation caused by the earthquake doublet, providing accurate imaging coseismic slip distributions on ruptured faults. Research shows that the majority of the slip of the doublet occurred at depths shallower than 15 km, with notably heterogeneous slip distributions (Barbot et al., 2023; He et al., 2023; Jia et al., 2023; Liu et al., 2023; Ma, Li, et al., 2024; Ren et al., 2024). Multiple major slip patches, where peak slip exceeded 7 m, were observed on the Pazarcık, Erkenek, and Çardak segments, while secondary patches dominated the slip pattern on the Amanos and Savrun segments. Additionally, Coulomb stress calculations indicate that slip on the EAF has increased the stress on the Çardak faults, potentially promoting the Mw7.7 event (He et al., 2023; Jia et al., 2023; Liu et al., 2023). However, kinematic rupture models in the literature display significant discrepancies, particularly regarding the speed of rupture propagation. For instance, Abdelmeguid et al. (2023), Liu et al. (2023), Ren et al. (2024) and Chen et al. (2024) argued that the northeast propagating rupture in the Mw7.8 event could reach super-shear speed, while many others (Delouis et al., 2024; Jia et al., 2023; Melgar et al., 2023; Xu et al., 2023; Zhang et al., 2023) suggested it was sub-shear. For the southwest propagating rupture, Zhang et al. (2023) reported a sustained super-shear rupture on the Amanos segment, whereas most other research contends that this segment primarily hosted sub-shear rupture. Additionally, it is well-established that the westward-propagating rupture of the bilateral Mw7.7 event was super-shear, supported by strong evidence from near-field strong motion and high-rate GPS stations located west of the rupture. However, the nature of the eastward-propagating rupture remains inconclusive, with studies such as Jia et al. (2023), Melgar et al. (2023), and Zhang et al. (2023) suggesting it was sub-shear, while Chen et al. (2024) and Liu et al. (2023) argue for a super-shear propagation.

In this study, we resolve the kinematic processes of the Mw7.8 and Mw7.7 earthquake doublet to explore the extent to which fault zone heterogeneities contribute to realistic earthquake dynamics. Using a path-calibrated teleseismic BP (Zeng et al., 2022), we trace the evolution of high-frequency radiation associated with the doublet. We highlight the noteworthy agreement between our BP results and near-fault strong motion observations, as well as surface rupture. Leveraging prior constraints from BP and near-fault strong motion data analyses, we conduct joint finite fault inversions using 3D surface deformation data (Ma, Li, et al., 2024), teleseismic body waves, and data from near-fault to regional strong motion and high-rate GNSS stations. Our finite fault models successfully reproduce near-fault to regional data up to 0.5 Hz. Additionally, waveform observations from a station pair located on opposite sides of the Amanos segment illustrate the presence of fault zone head waves due to material contrast across the EAF. Our findings reveal that the Mw7.8 earthquake primarily involves an asymmetric bilateral rupture, with part of the northeastward rupture reaching a super-shear speed (~5.2 km/s), while the southwestward rupture propagates primarily at the generalized Rayleigh speed (~3.4 km/s). This behavior underscores the role of inhomogeneity of the fault zone in earthquake dynamics. Conversely, the Mw7.7 event exhibits a bilateral super-shear rupture. Our findings suggest that in addition to geometrical and pre-stress heterogeneities, fault zone heterogeneities significantly influence the complexity of rupture dynamics.

2. Data and Methods

2.1. Teleseismic Back-Projection

To resolve the spatial-temporal evolution of the high-frequency (HF) (0.3–1.0 Hz, Figure S2 in Supporting Information S1) radiation of the doublet, we conduct the back-projection (BP) analysis using teleseismic array records (Figure 2a inset) (Text S1 in Supporting Information S1). BP takes advantage of source-receiver reciprocity and back-propagates the array HF waveform data to the source region, tracing the location and time of sources by either maximizing the stacking power in time domain (Ishii et al., 2005) or the coherence in frequency domain (Yao et al., 2011). However, the BP results may suffer from large uncertainties because the travel time, which is used to back-propagate HF waveforms, calculated using a 1D velocity model may not be accurate due to 3D source-side velocity structure (Zeng et al., 2022). To lessen the effects of source-side 3D structures on travel time calculations, we adopt a travel-time path calibration scheme, in which travel time correction is made by using the travel time of well-relocated, or calibration, events in the source region (Zeng et al., 2022).

This method starts by calibrating travel times from the source region to a teleseismic array using travel time measurements from intermediate magnitude (e.g., M5.5–6.5) events near the target (large) events, followed by the path-calibrated back-projection. For calibration, we select three events located in the rupture area of the doublet (Figure S1a in Supporting Information S1). We relocate large aftershocks and the epicenters of the doublet with BP to validate the calibrated BP method. As shown in Figures S1b and S1d in Supporting Information S1, the BP-inferred locations of these events closely match their catalog locations (Ding et al., 2023; Lomax, 2023), with average and maximum deviations of 7 and 11.5 km, respectively. We consider this average deviation as the BP location uncertainty (Zeng et al., 2022). The BP-derived HF radiation evolution for the doublet, represented by the locations and timings of HF radiators, is illustrated in Figure 2a. Most HF radiators are located within 10 km of the ruptured fault traces, consistent with the BP location uncertainty of ~7 km.

To determine the propagation distance of the HF radiators and, consequently, the rupture speeds, we orthogonally project the HF radiators onto a simplified version of the fault surface traces (Figure S6 in Supporting Information S1). We then measure the distance of these projected HF radiators along the fault surface traces relative to a reference point—the junction of the Narlı fault and the Pazarcık segment for the Mw7.8 event, and the epicenter for the Mw7.7 event, respectively. Figure S1e in Supporting Information S1 provides a conceptual illustration of this projection and distance measurement process. For the Mw7.8 event, HF radiators occurring within the first 18 s are projected onto the Narlı fault. The temporal progression of these HF radiators is illustrated in Figures 2b–2d. Notably, we observe spatial clustering of BP radiators in the map-view plot. For instance, BP radiators appear to stagnate near the epicenter of the Mw7.7 event for ~7 s (Figures 2a and 2c). Based on waveform analyses and synthetic tests (Text S1 in Supporting Information S1), we show that the stagnation is due to the finite length of coherent wave trains in the used waveforms.

We further validate the BP results using dense near-fault velocity waveforms from strong motion stations along the EAF. We also orthogonally project the strong motion stations (triangles in Figure 2a) onto the Amanos fault trace, and their velocity waveforms are sorted by distance along the fault and plotted alongside BP results

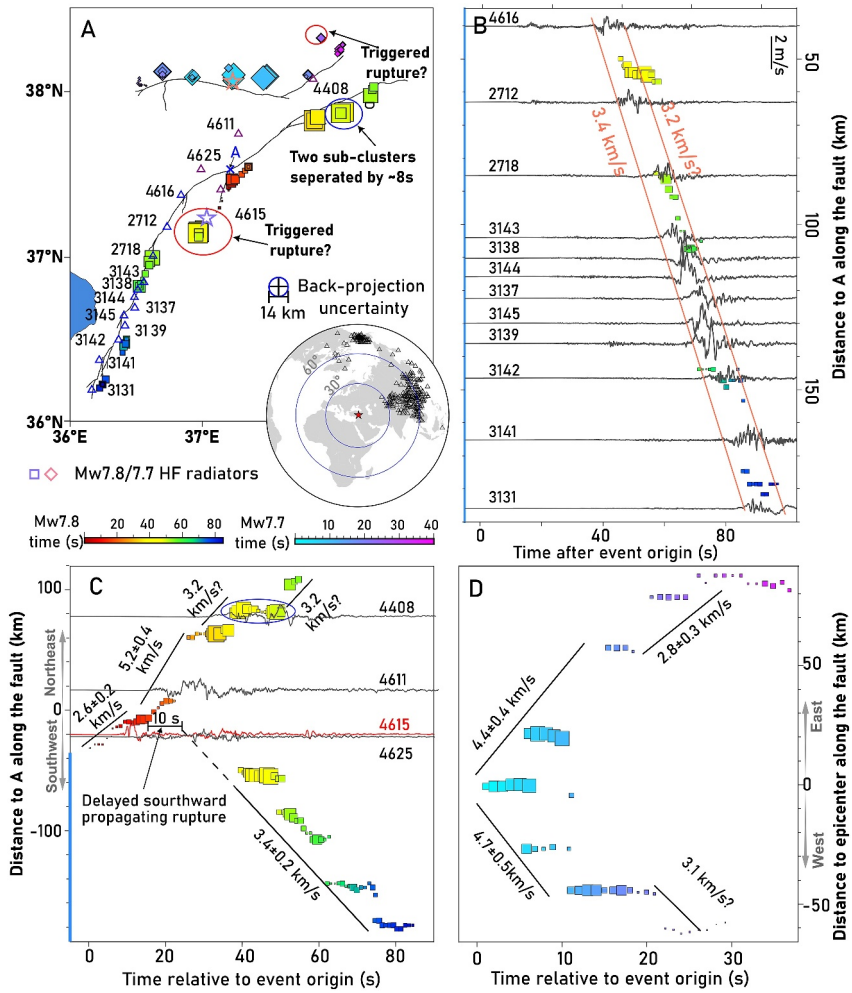

Figure 2. High-frequency radiation evolution of the Turkey doublet. (a) Map view of the back-projection (BP) results showing BP radiators for the Mw7.8 and Mw7.7 events as squares and diamonds, respectively, sized by normalized BP power and colored by time (see color bars). Purple and blue triangles mark near-fault strong motion stations that recorded signals from the Mw7.8 event, with corresponding waveforms displayed in (b) and (c). Point A, the junction of the Narlı fault and the Pazarcık segment, serves as reference (0 km) for measuring distances along the fault for the Mw7.8 event. The lower-right inset displays the distribution of teleseismic stations used in the BP analysis. (b) Fault parallel (FP) waveforms along the Amanos segment from near-fault stations shown in (a), with stations projected to the fault line and distances measured relative to reference point A. BP results are similarly plotted. Two red lines trace the onset and cessation of the velocity pulses recorded by the near-fault strong motion stations. The vertical bar labeled '2 m/s' represents the scale of the fault-parallel velocity motion. (c)–(d) Relationship between BP timing and distances from BP radiators to reference points along fault lines for the Mw7.8 and Mw7.7 events, respectively. The reference location for the Mw7.7 event is its epicenter.

(Figures 2b, 2c and S4 in Supporting Information S1). The HF radiator locations and timings along the Amanos segment align well with the strong motion data (Figure 2b). For instance, a cluster of HF radiation at 50–55 s near station 2,718 corresponds to a rupture pulse (50–56 s) in the strong motion waveforms. The consistency between BP results and near-fault strong motion records strengthens our confidence in reconstructing rupture processes of the doublet.

2.2. Finite Fault Model

We resolve the coseismic slip evolution of the doublet by conducting Finite Fault Model (FFM) (Ji et al., 2002) with a joint inversion of seismic and 3D surface deformation data (Figure 1b). The seismic data include near-fault to regional strong motion and 1-Hz regional high-rate GPS (Figure 1a and Figure S6 in Supporting Information S1) waveforms, along with teleseismic body waves. The 3D surface deformation field is down-sampled from

that in Ma et al. (2024a) (Text S3 in Supporting Information S1). We derive a simplified version of the fault geometry constrained by the geodetic data (Ma, Li, et al., 2024) and surface rupture traces (Reitman et al., 2023), and we use 7 and 4 fault segments to approximate the ruptured faults of the Mw7.8 and 7.7 events, respectively (Figure S6 in Supporting Information S1). The dip angles of these segments roughly align with those determined in Ma et al. (2024a). Additionally, we conduct waveform modeling of a Mw6.3 aftershock to constrain the shallow crust velocity structure, which is crucial for calculating Green's Functions in the inversion (Text S3 in Supporting Information S1), and to compare the shallow shear wave speeds with the rupture speeds. The optimal crust velocity model is shown in Figure S7 in Supporting Information S1.

Throughout the inversion process, to reduce trade-offs between model parameters, we have refined the search space for rupture speed history based on BP and near-fault strong motion waveform analyses. For the Mw7.8 event, the speeds of the northeastward and southeastward propagating ruptures are constrained to be centered around the speed from BP analysis (mostly ± 0.5 km/s). For the Mw7.7 event, the rupture speed is specifically limited between 3.0 and 5.5 km/s. Notably, for the Mw7.8 event, we have introduced a prescribed delay of 10 s for the southward propagating rupture relative to the northward propagation, as evidenced by BP and near-fault strong motion waveform analyses (refer to Figure 2c and S5b in Supporting Information S1).

3. Results

3.1. Rupture Processes Inferred From Teleseismic Back-Projection

Our BP results indicate that the Mw7.8 event initiated on the Narlı fault at a speed of ∼2.6 km/s and propagated northeastward to the Pazarcık segment on the main EAF. Near-fault strong motion stations close to the Narlı fault recorded dominant fault-parallel over fault-normal velocity waveforms, suggesting that the rupture likely transitioned to super-shear speed after initially propagating at sub-Rayleigh speeds for the first 19.5 km, near station 4,615, just before intersecting the EAF (Abdelmeguid et al., 2023; A Rosakis et al., 2023). The rupture then propagated bilaterally along the EAF, moving northeast into the compressional quadrant and southwest into the dilatational quadrant of the left-lateral Narlı fault rupture, upon reaching the Pazarcık segment.

The northeastward rupture maintained a super-shear speed of ∼5.2 km/s for ∼60 km before slowing near the Pazarcık and Erkenek segments junction, transitioning to slower rupture at ∼3.2 km/s on the Erkenek segment before stopping. The southwestward rupture, delayed by ∼10 s compared to the northeastward rupture, propagated ∼25 km on the Pazarcık segment and ∼155 km on the Amanos segment at a stable speed of ∼3.4 km/s. The delayed rupture may have been caused by that the northeastward rupture initially posed a dynamic barrier on the backward segment, but subsequently generated dynamic unclamping, transient shear stressing, and static stress buildup (Jia et al., 2023). These factors eventually led to the rupture of the southwest segment. Additionally, data from near-fault strong motion stations 4,624 and 4,625 suggest the southwestward rupture reached 3.3–3.5 km/s within 25 km of the Narlı fault and Pazarcık segment junction (Text S2 and Figure S5c in Supporting Information S1). Tracing the initiation of velocity pulses recorded by near-fault waveforms (Figure 2b and Figure S4 in Supporting Information S1) also derives a speed of 3.4 km/s for the southwest propagating rupture, consistent with BP result. This speed is roughly 9% larger than the Rayleigh wave speed (∼3.1–3.2 km/s, considering a shear wave speed of 3.4–3.5 km/s, representative of the shear wave velocity at 5–10 km depth in our preferred velocity model constrained by waveform modeling (Figure S7 in Supporting Information S1)), the canonical speed of a stable strike slip rupture in a homogenous fault zone, suggesting a "super-Rayleigh" speed. At ∼ 45 s, a HF radiation cluster burst southwest of the epicenter. Given that intense aftershocks occurred near this cluster (Figure S1c in Supporting Information S1), it likely represents a triggered rupture on the Narlı fault, activated by the dynamic stress associated with the rupture on the Amanos segment.

Several other key features of the Mw7.8 rupture process are further corroborated by near-fault strong motion records. For example, if the super-shear rupture initiated near station 4,615 and propagated northeastward without deceleration until rupturing the Erkenek fault, a predicted Mach cone should arrive at station 4,611 ∼20 s after the event origin, aligning well with the large-amplitude arrival recorded there (Figures S5a and S5b in Supporting Information S1). Additionally, assuming no delay in the southwestward rupture initiation, the predicted arrival at station 4,616 would be ∼24 s after the origin, ∼8 s earlier than observed (Figure S5b in Supporting Information S1), suggesting an ∼8-s delay in southwestward rupture initiation, consistent with the BP analysis-derived delay of ∼10 s. Near station 4,408, HF radiators show two temporal sub-clusters separated by ∼8 s (highlighted by blue ellipses in Figures 2a and 2c). The waveforms recorded by this station also show two rupture

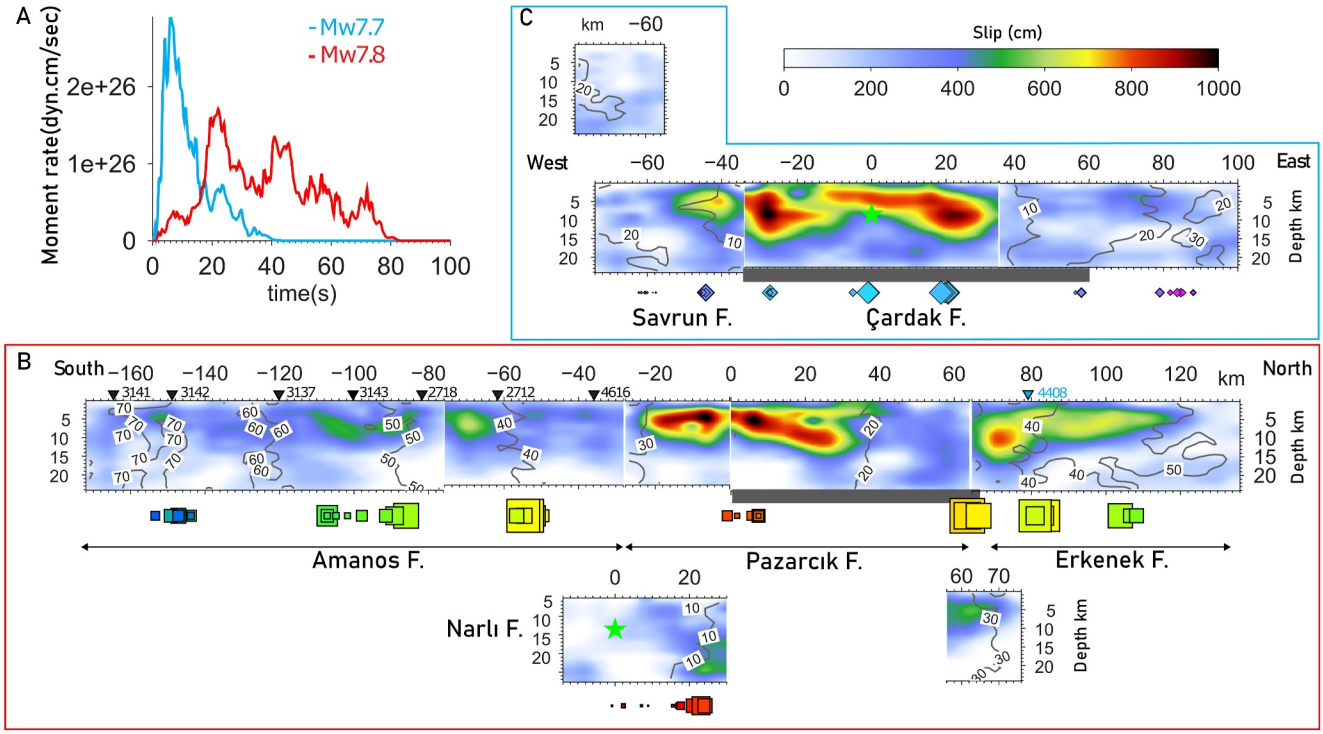

Figure 3. Finite fault models and representative waveform fittings for the doublet. (a) Moment-rate function of the doublet. (b) Depth profile of the rupture model for the Mw7.8 event, with the hypocenter marked by a green star. Selected stations along the Amanos segment are shown as triangles, labeled with station IDs; their waveform fittings are presented in Figure 4. (c) Rupture model of the Mw7.7 event. In panels (b) and (c), gray bars highlight the major fault segments hosting super-shear ruptures. High-frequency radiators are placed at bottom of the rupture models.

pulses with similar separation (Figure S5d in Supporting Information S1). By comparing the strong motion data (Figure S5d in Supporting Information S1), BP result (Figure 2c), and finite fault model (Section 3.2 and Figure 3), the observed double-pulse feature can be attributed to cascading failure of deeper and shallower slip patches near station 4,408.

The Mw7.7 earthquake originated at the center of the Çardak fault, and then propagated both eastward and westward simultaneously (Figures 2a and 2d). The rupture quickly transitioned to super-shear speed in both directions. The eastward rupture traveled at ~4.4 km/s for ~40 km, then continued northeastward at the same speed for an additional ~20 km before slowing to ~2.8 km/s for another ~20 km. The westward rupture maintained a speed of ~4.7 km/s for ~45 km before decelerating to ~3.1 km/s on the Savrun fault, where it eventually stopped ~20 km further west.

3.2. Coseismic Slip Evolution

The preferred finite fault models of the doublet are presented as depth profiles in Figure 3 (slip) and S14 (rise time and average slip rate defined as the ratio between slip and rise time). The snapshots of the coseismic slip evolution for the doublet are also shown in Figures 5 and 6. These models produce excellent fits to the strong motion data (Figure 4, S8, and S11 in Supporting Information S1), the 3D surface deformation field (Figures S10 and S13 in Supporting Information S1), high-rate GPS data (Figures S8 and S11 in Supporting Information S1), and teleseismic waveforms (Figures S9 and S12 in Supporting Information S1). Especially, for the Mw7.8 event, near-fault strong motion waveforms are well-matched up to 0.5 Hz (Figure 4 and S8 in Supporting Information S1). Considering that the rupture speed constraints in finite fault inversion are primarily guided by the BP results, such reconciliation provides further confidence in both FFM and BP results.

The Mw7.8 event lasted ~80 s—twice the duration of the Mw7.7 event—with its peak moment rate about half that of the Mw7.7 event (Figure 3a). Both events featured heterogeneous slip distributions. We observed dominant slip patches with peak slip exceeding 7 m on the Pazarcık, Erkenek, and Çardak faults, and secondary slip patches with

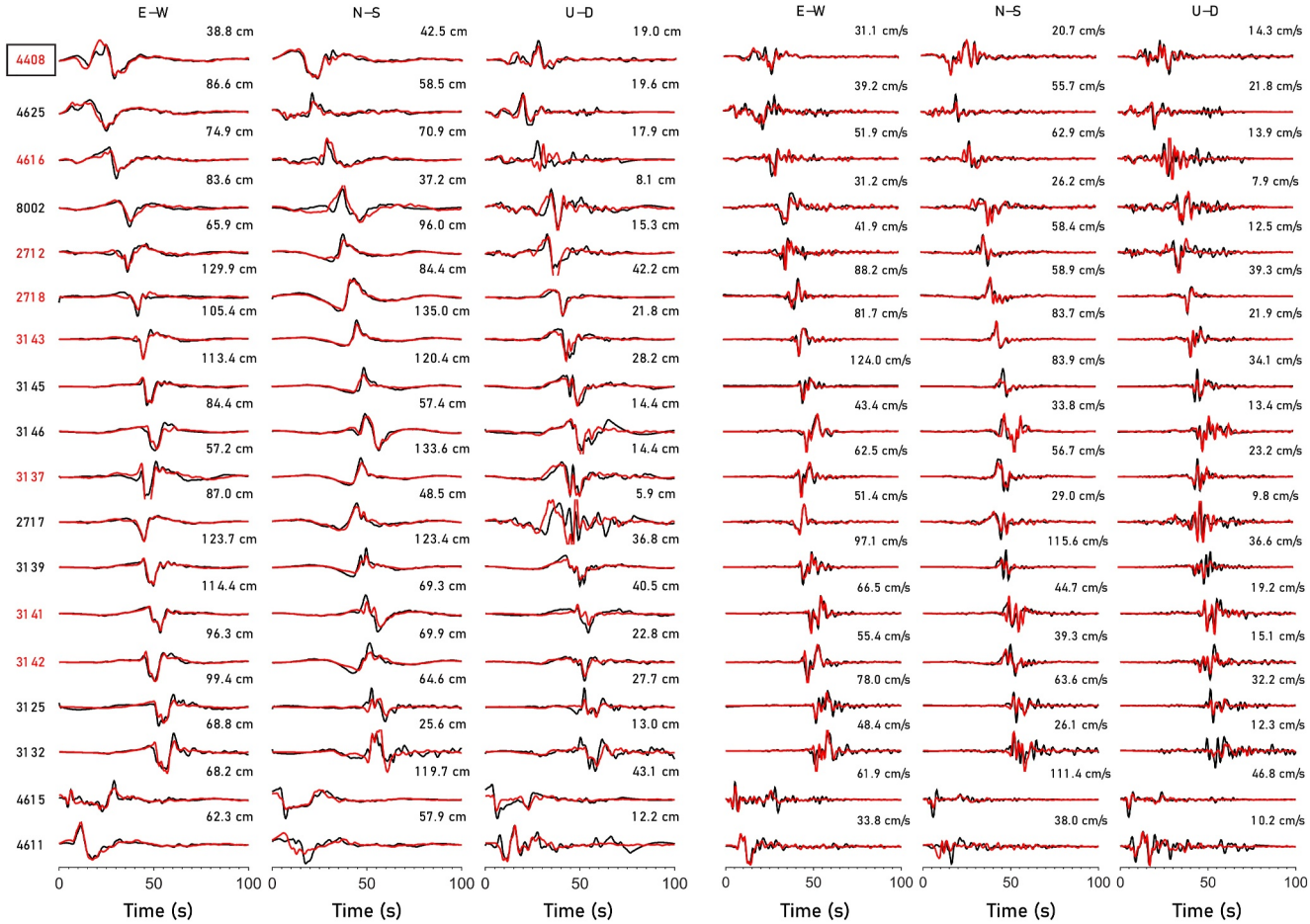

Figure 4. Near-fault strong motion waveform fitting for the Mw7.8 event, presented in displacement (left) and velocity (right). Observed data are shown in black, and synthetics are in red, filtered between 0.02 and 0.5 Hz. The maximum amplitude of the data is indicated at the end of each waveform pair. Stations with red station IDs correspond to those shown in Figure 3c. Station 4,408 is prominently displayed at the top, located near the Erkenek segment north of the epicenter. The broadband velocity waveforms recorded by station 4,408 are shown in Figure S5d in Supporting Information S1. The locations of these stations can be found in Figure 1 and S6 in Supporting Information S1.

peak slip around 6 m on the Amanos and Savrun faults. Most of the slip occurred at shallow depths (<10 km), with significant deeper slips (>10 km) observed on the Pazarcık, Erkenek, and Çardak faults. Especially, the identified super-shear ruptures occurred on fault segments with larger slip amplitude and longer rise time (Figures 3b, 3c, and S14 in Supporting Information S1), suggesting significant dynamic weakening during these ruptures.

Comparison between the HF radiator location and coseismic slip distribution suggests that HF energy is primarily radiated from the edges of slip patches and areas where the fault geometry changes (Figures 2 and 3), consistent with observations made for other earthquakes (Avouac et al., 2015; Lay et al., 2012; Ma, Zeng, et al., 2024; Uchide et al., 2013; Wei et al., 2022). In addition, the snapshots of coseismic slip and HF radiation suggest that generally the HF radiation precedes coseismic slip (Figures 5 and 6). However, given the overall short rise time (less than 10 s) and the finite length (~10 s) of the coherent train of HF waveforms (Figure S2 in Supporting Information S1), it is challenging to discuss unambiguously how the rupture front is followed by slip. Such analysis for a megathrust event (e.g., the 2011 Mw9.1 Tohoku-Oki earthquake (Wei et al., 2012)), which features longer rise times for slip on a fault patch, could better illustrate the relationship between rupture front and slip.

The super-shear segments identified in this study coincide with areas that experienced widespread off-fault building damage (Yu et al., 2024). This correlation suggests that high rupture speeds likely contribute to intense ground shaking and consequently, severe seismic hazards. For the northeast-propagating rupture of the Mw7.8 event, our findings indicate it reached super-shear speed along the Narlı and Pazarcık faults. This aligns with the results presented by Abdelmeguid et al. (2023), Chen et al. (2024) and Ren et al. (2024), although the

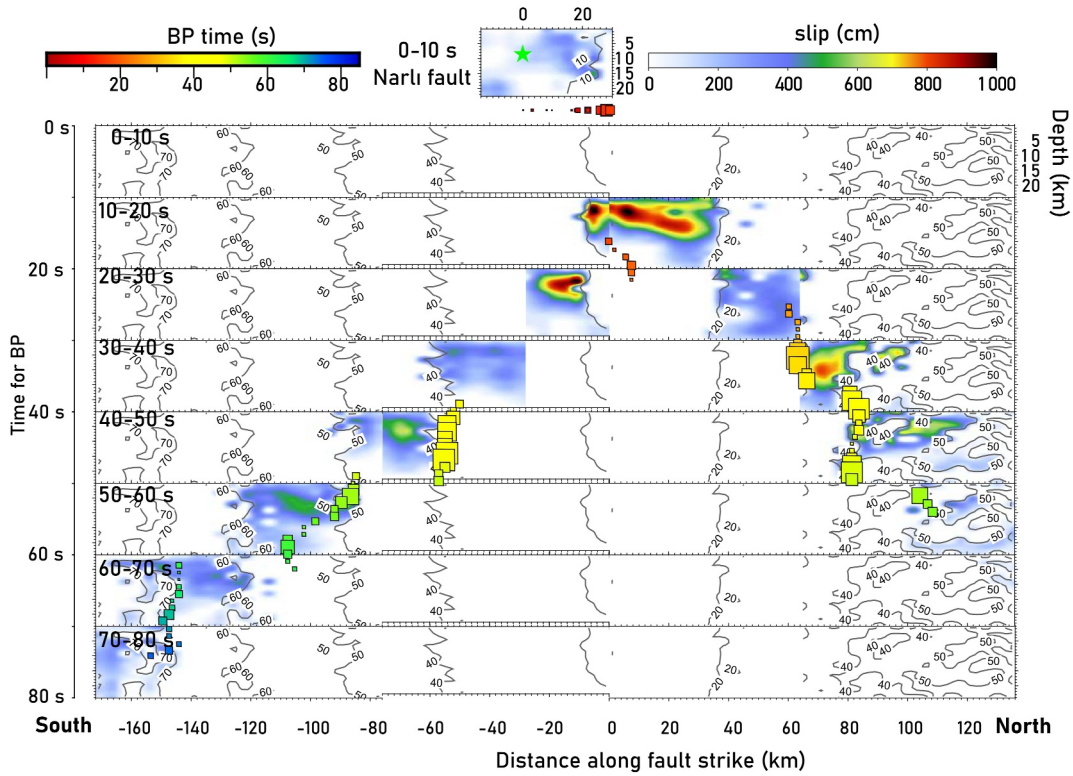

Figure 5. Spatial-temporal evolution of the coseismic slip and high-frequency (HF) radiation (squares) for the Mw7.8 event. Snapshots are taken at 10-s intervals. We only display the slip on the Narlı fault in the 0-10-s snapshot, as there is almost no slip observed after 10 s. HF radiators located on the Narlı fault are displayed on the bottom of the coseismic slip.

exact values of rupture speeds differ. Liu et al. (2023) and Wang et al. (2023) reported that super-shear occurred on the Erkenek and Pazarcık segment, respectively. In contrast, most other studies suggest a sub-shear speed for this rupture (Delouis et al., 2024; Jia et al., 2023; Melgar et al., 2023; Xu et al., 2023; Zhang et al., 2023).

For the southwest-propagating rupture of the Mw7.8 event, our analysis, along with most other studies (Chen et al., 2024; Delouis et al., 2024; Jia et al., 2023; Liu et al., 2023; Mai et al., 2023; Melgar et al., 2023; Xu et al., 2023), resolves it to be dominantly sub-shear, although localized super-shear rupture over the last ∼50 km have been suggested by Abdelmeguid et al. (2023), Liu et al. (2023) and Wang et al. (2023). The predominantly sub-shear rupture contrasts with Zhang et al. (2023), who argue for a sustained super-shear rupture propagating southwest.

For the Mw7.7 event, data from near-field strong motion and high-rate GPS stations provide strong constraints on the west-propagating rupture. Our waveform modeling of the strong motion station data suggests a super-shear rupture speed of ∼4.7 km/s for the westward rupture (Figure S15 in Supporting Information S1), consistent with most other analyses of near-field to regional seismological and high-rate GPS data (Chen et al., 2024; Jia et al., 2023; Liu et al., 2023; Melgar et al., 2023; Ren et al., 2024). However, there are discrepancies regarding whether the eastward-propagating rupture is super-shear. We argue that these discrepancies are mainly due to the data used. In our analysis, along with Liu et al. (2023)'s and Chen et al. (2024)'s studies, a super-shear eastward propagation can improve the fit to data (up to ∼0.5 Hz in our study) from strong motion (e.g., station 4,406 in Figures S11 and S15 in Supporting Information S1) and high-rate GPS stations closest to the fault to the east. In contrast, other studies favoring a sub-shear rupture either neglect these data, use them at lower frequencies, or achieve a less optimal fit (Jia et al., 2023; Melgar et al., 2023; Ren et al., 2024; Zhang et al., 2023).

4. Discussion and Conclusion

The doublet exhibits complex rupture dynamics, which can be influenced by factors such as stress and geometry heterogeneities in the fault zone, coseismic dynamic/static stress loading, and static stress interactions between

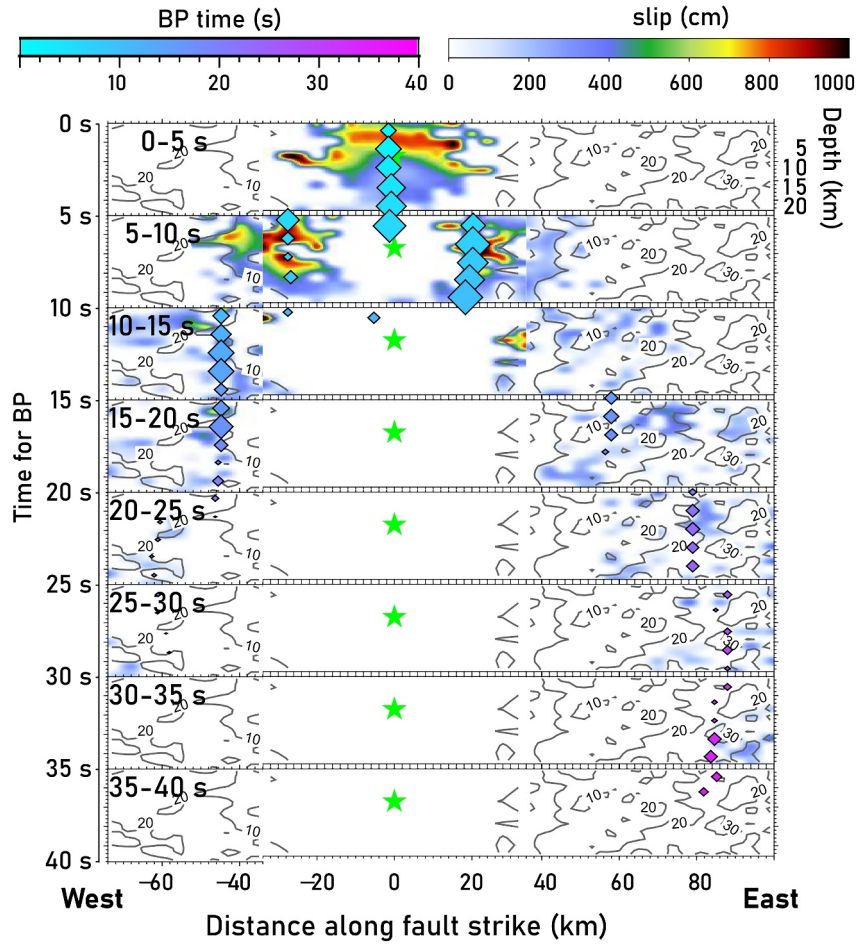

Figure 6. Spatial-temporal evolution of the coseismic slip and high-frequency (HF) radiation (diamonds) for the Mw7.7 event. Snapshots are taken at 5-s intervals.

the two earthquakes (Abdelmeguid et al., 2023; Jia et al., 2023; Liu et al., 2023; Toda et al., 2023). In particular, the Mw7.8 event features asymmetric rupture speeds and a "super-Rayleigh" rupture along the Amanos segment. We propose that material contrast across the East Anatolian Fault (EAF) also significantly contributes to the complexity of these dynamics.

Besides evidence from attenuation (Zhu et al., 2023) (Figure S16a in Supporting Information S1), shear wave speed (Delph et al., 2017; Rodgers et al., 2024) (Figure S16b in Supporting Information S1), and crustal thickness (Ogden & Bastow, 2022) contrasts across EAF, we demonstrate that Fault Zone Head Wave (FZHW) observations support that the separates the more compliant East Anatolian plate and the harder Arabian plate. FZHWs propagate along the fault interface and refract toward seismic stations in the slower medium, and these waves typically have an emergent onset and inverted polarities compared to direct P waves (Figure 7a inset) (Ben-Zion & Malin, 1991). We analyze seismic waveforms from two adjacent stations located on opposite sides of the Amanos fault (stations KAMA and 2,712, shown in Figure 7a). We first compare waveforms with positive polarity at both stations, which correspond to a left-lateral strike-slip focal mechanism. Limited data availability from station 2712 restricts our comparison to only four waveform pairs.

Overall, waveforms at station 2712 have a more impulsive onset compared to those at station KAMA (Figure 7c), indicating FZHWs recorded by station KAMA and therefore a slower seismic wave velocity on the western side of the Amanos fault (i.e., East Anatolian plate). The time separation (Δt) between FZHWs and the first P waves increases with the distance to station KAMA, demonstrating a FZHW moveout (Figure 7b). This moveout suggests a material contrast of ∼8% across the Amanos fault (Text S4 more in Supporting Information S1) (Ben-

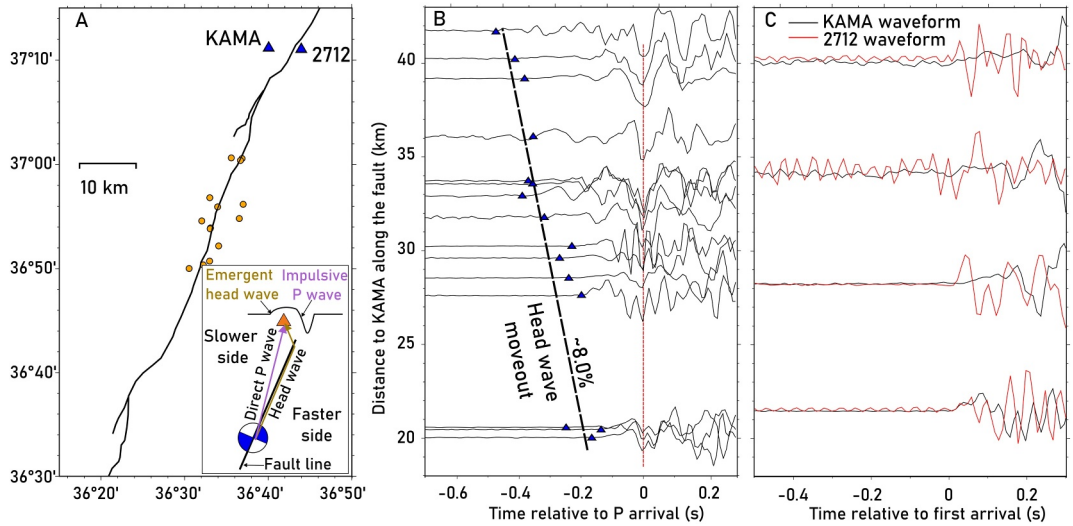

Figure 7. Fault Zone Head Waves (FZHWs) observations. (a) Seismic stations (blue triangles) and seismicity (brown circles) used to detect potential Fault Zone Head Waves (FZHWs). The inset shows how FZHWs are generated. (b) Potential FZHWs recorded at station KAMA, with their arrivals marked by blue triangles. The linear FZHW moveout suggests that the seismic wave speed of the East Anatolian plate is approximately 8% slower than the average seismic wave speed of the Arabian and East Anatolian plates. (c) Comparison of waveforms recorded at stations KAMA and 2,712. All waveforms displayed for station 2,712 feature positive polarity, consistent with a left-lateral strike-slip focal mechanism. Although the stations are in close proximity, station KAMA recorded more emergent first arrivals compared to those at station 2,712, indicating the presence of FZHWs.

Zion & Malin, 1991). While the accuracy of material contrast estimations may be refined in future studies, our observations align with other findings indicating substantial material contrast across the Amanos fault.

Therefore, based on the material contrast and the left-lateral motion of the earthquake slip, the southward and northeastward directions are the positive and negative directions (see the definition in the Section 1) in the bi-material EAF fault zone, respectively, aligning well with the observed asymmetrical propagation speeds of the Mw7.8 rupture (Figure 8). In the absence of material contrast, a "super-Rayleigh" rupture speed of ~3.4 km/s in the southwest direction would be mechanically unfavorable for a strike-slip (mode-II) rupture due to

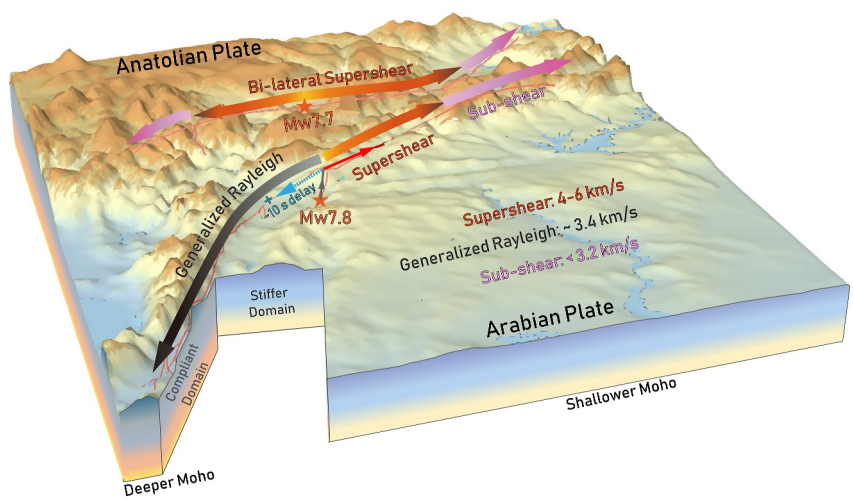

Figure 8. Cartoon depicting the overall rupture speeds of the doublet, with sub-shear, generalized Rayleigh, and super-shear ruptures indicated by purple, black, and red arrows, respectively. Stars mark the epicenters of the doublet. The symbols (+) and (−) represent positive and negative directions in a bi-material rupture scenario, where the positive direction is the moving direction of the more compliant material, and the negative direction is the opposite.

unrealistic energy flux near the rupture tip (Freund, 1979). However, with a 10%–20% shear-wave speed contrast across the fault, a generalized Rayleigh speed of 3.3–3.4 km/s becomes favorable along the positive direction. Conversely, the northeastward rupture on the Pazarcik segment, propagating along the negative direction, traveled at a super-shear speed of 5.2 km/s, as also reported by Abdelmeguid et al. (2023) for the same segment. While less frequent, rupture in the positive direction can still transition into super-shear speed (Sammis et al., 2010), albeit with a much longer transition length compared to a homogeneous scenario [Bhat et al., 2010; A. J. Rosakis et al., 2007]. The late transition may explain the possible localized super-shear rupture along the positive direction occurring in the last 50 km of the Amanos segment (Abdelmeguid et al., 2023; Liu et al., 2023; Wang et al., 2023).

In contrast, the intraplate fault zone hosting the Mw7.7 event exhibits moderate material contrast (Figure 8 and S16b in Supporting Information S1), facilitating the bilateral super-shear rupture, as shown in BP and FFM results. The near-instantaneous development of bilateral super-shear suggests a short transition length from sub-Rayleigh to super-shear rupture, indicating high pre-stress condition (Burridge et al., 1979; Das & Aki, 1977a; A. J. Rosakis et al., 2007; Xia et al., 2004). This observation aligns with the extended quiescent period of the Çardak fault and the substantial coseismic slip of the earthquake.

In conclusion, our study highlights that the velocity structure within the fault zone can play a dominant role in the development of complex ruptures. Unique slip-stress interactions introduced by the bi-material fault zone substantially impact rupture dynamics, promoting super-shear in some directions and retarding it in others, thereby affecting ground shaking characteristics along various parts of the fault.

Data Availability Statement

The ground motion data used in this study can be obtained from Turkish Disaster and Emergency Management Authority AFAD, US Geological Survey (USGS), and Kandilli Observatory and Earthquake Research Institute. The authors thank Turkey's General Directorate of Land Registry and Cadastre and General Directorate of Maps for making the 1-Hz GNSS RINEX data available from the CORS-TR (TUSAGA-Aktif-Türkiye) GNSS network. We use the publicly available seismic data from the following networks: AK (Alaska Earthquake Center, 1987), AV (Alaska Volcano Observatory/USGS, 1988), CN (Natural Resources Canada, 1975), DK (GEUS Geological Survey of Denmark and Greenland, 1976), G (IPGP & EOST, 1982), IC (ASL/USGS, 1992), II (Scripps Institution of Oceanography, 1986), IU (ASL/USGS, 1988), JP, KG, KR (Kyrgyz Institute of Seismology, KIS, 2007), KS, MM (Department of Meteorology and Hydrology - National Earthquake Data Center, 2016), PS, PQ (Geological Survey of Canada, 2013), RM (RIMES Thailand, 2008), RV (Alberta Geological Survey / Alberta Energy Regulator, 2013), TM, TW (Institute of Earth Sciences et al., 1996), US (ASL/USGS, 1990). We also use seismic data from the Second Monitoring and Application Center, CEA.

Acknowledgments

We thank the associate editor and two anonymous reviewers for their comments, which have improved the quality of the paper. This research was supported by Singapore MOE project (MOE-T2EP50124-0011). The authors thank Dr. Suli Yao and Dr. Hongfeng Yang at the Chinese University Hong Kong. The authors thank the PRIDE Lab in the GNSS Research Center of Wuhan University for producing the high-rate GNSS time series. Finally, A.J.R. acknowledges support by the Caltech/MCE Big Ideas Fund (BIF), the Caltech Terrestrial Hazard Observation and Reporting Centre (THOR) and of NSF (Grant EAR-2045285). All the figures are generated by the Generic Mapping Tool (GMT), the seismic data are processed using SAC and the python package, Obspy.

References

Abdelmeguid, M., Zhao, C., Yalcinkaya, E., Gazetas, G., Elbanna, A., & Rosakis, A. (2023). Dynamics of episodic supershear in the 2023 M7. 8 Kahramanmaraş/Pazarcik earthquake, revealed by near-field records and computational modeling. *Communications Earth and Environment*, *4*(1), 456. https://doi.org/10.1038/s43247-023-01131-7

Adams, G. (2001). An intersonic slip pulse at a frictional interface between dissimilar materials. *Journal of Applied Mechanics*, *68*(1), 81–86. https://doi.org/10.1115/1.1349119

Aktug, B., Ozener, H., Dogru, A., Sabuncu, A., Turgut, B., Halicioglu, K., et al. (2016). Slip rates and seismic potential on the East Anatolian Fault System using an improved GPS velocity field. *Journal of Geodynamics*, *94*, 1–12. https://doi.org/10.1016/j.jog.2016.01.001

Alaska Earthquake Center, Univ. of Alaska Fairbanks. (1987). Alaska geophysical network. *International Federation of Digital Seismograph Networks*. [Dataset]. https://doi.org/10.7914/SN/AK

Alaska Volcano Observatory/USGS. (1988). Alaska Volcano Observatory. *International Federation of Digital Seismograph Networks*. [Dataset]. https://doi.org/10.7914/SN/AV

Alberta Geological Survey / Alberta Energy Regulator. (2013). Regional Alberta observatory for earthquake studies network. *International Federation of Digital Seismograph Networks*. [Dataset]. https://doi.org/10.7914/SN/RV

Albuquerque Seismological Laboratory (ASL)/USGS. (1990). United States national seismic network. *International Federation of Digital Seismograph Networks*. [Dataset]. https://doi.org/10.7914/SN/US

Albuquerque Seismological Laboratory (ASL)/USGS. (1992). New China digital seismograph network. *International Federation of Digital Seismograph Networks*. [Dataset]. https://doi.org/10.7914/SN/IC

Albuquerque Seismological Laboratory/USGS. (1988). Global seismograph network (GSN - IRIS/USGS). *International Federation of Digital Seismograph Networks*. [Dataset]. https://doi.org/10.7914/SN/IU

Avouac, J. P., Meng, L. S., Wei, S. J., Wang, T., & Ampuero, J. P. (2015). Lower edge of locked main Himalayan thrust unzipped by the 2015 Gorkha earthquake. *Nature Geoscience*, *8*(9), 708–711. https://doi.org/10.1038/Ngeo2518

Balkaya, M., Akyüz, H. S., & Özden, S. (2023). Paleoseismology of the Sürgü and Çardak faults-splays of the eastern Anatolian Fault Zone, Türkiye. *Turkish Journal of Earth Sciences*, *32*(3), 402–420.

Bao, H., Xu, L., Meng, L., Ampuero, J.-P., Gao, L., & Zhang, H. (2022). Global frequency of oceanic and continental supershear earthquakes. *Nature Geoscience*, *15*(11), 942–949. https://doi.org/10.1038/s41561-022-01055-5

Barbot, S., Luo, H., Wang, T., Hamiel, Y., Piatibratova, O., Muhammad, T., et al. (2023). Slip distribution of the February 6, 2023 Mw 7.8 and Mw 7.6, Kahramanmaraş, Turkey earthquake sequence in the East Anatolian Fault Zone. *Seismica*, *3*(2). https://doi.org/10.26443/seismica.v2i3.502

Ben-Zion, Y. (2001). Dynamic ruptures in recent models of earthquake faults. *Journal of the Mechanics and Physics of Solids*, *49*(9), 2209–2244. https://doi.org/10.1016/s0022-5096(01)00036-9

Ben-Zion, Y., & Malin, P. (1991). San Andreas fault zone head waves near Parkfield, California. *Science*, *251*(5001), 1592–1594. https://doi.org/10.1126/science.251.5001.1592

Bhat, H. S., Biegel, R. L., Rosakis, A. J., & Sammis, C. G. (2010). The effect of asymmetric damage on dynamic shear rupture propagation II: With mismatch in bulk elasticity. *Tectonophysics*, *493*(3–4), 263–271. https://doi.org/10.1016/j.tecto.2010.03.016

Burridge, R., Conn, G., & Freund, L. (1979). The stability of a rapid mode II shear crack with finite cohesive traction. *Journal of Geophysical Research*, *84*(B5), 2210–2222. https://doi.org/10.1029/jb084ib05p02210

Chen, K., Wei, G., Milliner, C., Dal Zilio, L., Liang, C., & Avouac, J.-P. (2024). Super-shear ruptures steered by pre-stress heterogeneities during the 2023 Kahramanmaraş earthquake doublet. *Nature Communications*, *15*(1), 7004. https://doi.org/10.1038/s41467-024-51446-y

Cochard, A., & Rice, J. (2000). Fault rupture between dissimilar materials: Ill-posedness, regularization, and slip-pulse response. *Journal of Geophysical Research*, *105*(B11), 25891–25907. https://doi.org/10.1029/2000jb900230

Das, S., & Aki, K. (1977a). Fault plane with barriers: A versatile earthquake model. *Journal of Geophysical Research*, *82*(36), 5658–5670. https://doi.org/10.1029/jb082i036p05658

Das, S., & Aki, K. (1977b). A numerical study of two-dimensional spontaneous rupture propagation. *Geophysical Journal International*, *50*(3), 643–668. https://doi.org/10.1111/j.1365-246x.1977.tb01339.x

Delouis, B., van den Ende, M., & Ampuero, J. P. (2024). Kinematic rupture model of the 6 February 2023 M w 7.8 Türkiye earthquake from a large set of near-source strong-motion records combined with GNSS offsets reveals intermittent supershear rupture. *Bulletin of the Seismological Society of America*, *114*(2), 726–740. https://doi.org/10.1785/0120230077

Delph, J. R., Abgarmi, B., Ward, K. M., Beck, S. L., Özacar, A. A., Zandt, G., et al. (2017). The effects of subduction termination on the continental lithosphere: Linking volcanism, deformation, surface uplift, and slab tearing in central Anatolia. *Geosphere*, *13*(6), 1788–1805. https://doi.org/10.1130/ges01478.1

Department of Meteorology and Hydrology - National Earthquake Data Center. (2016). Myanmar national seismic network. *International Federation of Digital Seismograph Networks*. [Dataset]. https://doi.org/10.7914/SN/MM

Ding, H., Zhou, Y., Ge, Z., Taymaz, T., Ghosh, A., Xu, H., et al. (2023). High-resolution seismicity imaging and early aftershock migration of the 2023 Kahramanmaraş (SE Türkiye) M W 7.9 and 7.8 earthquake doublet. *Earthquake Science*, *36*, 1–16.

Duman, T. Y., & Emre, Ö. (2013). The East Anatolian Fault: Geometry, segmentation and jog characteristics. *Geological Society, London, Special Publications*, *372*(1), 495–529. https://doi.org/10.1144/sp372.14

Dunham, E. M., & Bhat, H. S. (2008). Attenuation of radiated ground motion and stresses from three-dimensional supershear ruptures. *Journal of Geophysical Research*, *113*(B8). https://doi.org/10.1029/2007jb005182

Ekstrom, G., Nettles, M., & Dziewonski, A. M. (2012). The global CMT project 2004-2010: Centroid-moment tensors for 13,017 earthquakes. *Physics of the Earth and Planetary Interiors*, *200*, 1–9. https://doi.org/10.1016/j.pepi.2012.04.002

Freund, L. (1979). The mechanics of dynamic shear crack propagation. *Journal of Geophysical Research*, *84*(B5), 2199–2209. https://doi.org/10.1029/jb084ib05p02199

Gabriel, A. A., Ulrich, T., Marchandon, M., Biemiller, J., & Rekoske, J. (2023). 3D dynamic rupture modeling of the 6 February 2023, Kahramanmaraş, Turkey M w 7.8 and 7.7 earthquake doublet using early observations. *The Seismic Record*, *3*(4), 342–356. https://doi.org/10.1785/0320230028

Geological Survey of Canada. (2013). Public safety geoscience program Canadian research network. *International Federation of Digital Seismograph Networks*. [Dataset]. https://doi.org/10.7914/SN/PQ

Gerstenberger, M. C., Marzocchi, W., Allen, T., Pagani, M., Adams, J., Danciu, L., et al. (2020). Probabilistic seismic hazard analysis at regional and national scales: State of the art and future challenges. *Reviews of Geophysics*, *58*(2), e2019RG000653. https://doi.org/10.1029/2019rg000653

GEUS Geological Survey of Denmark and Greenland. (1976). Danish seismological network. *International Federation of Digital Seismograph Networks*. [Dataset]. https://doi.org/10.7914/nw3x-df02

Goldberg, D. E., Taymaz, T., Reitman, N. G., Hatem, A. E., Yolsal-Çevikbilen, S., Barnhart, W. D., et al. (2023). Rapid characterization of the February 2023 Kahramanmaraş, Türkiye, earthquake sequence. *The Seismic Record*, *3*(2), 156–167. https://doi.org/10.1785/0320230009

Hamling, I. J., Hreinsdóttir, S., Clark, K., Elliott, J., Liang, C., Fielding, E., et al. (2017). Complex multifault rupture during the 2016 M w 7.8 Kaikōura earthquake, New Zealand. *Science*, *356*(6334), eaam7194. https://doi.org/10.1126/science.aam7194

Harris, R. A., & Day, S. M. (1997). Effects of a low-velocity zone on a dynamic rupture. *Bulletin of the Seismological Society of America*, *87*(5), 1267–1280. https://doi.org/10.1785/bssa0870051267

He, L., Feng, G., Xu, W., Wang, Y., Xiong, Z., Gao, H., & Liu, X. (2023). Coseismic kinematics of the 2023 Kahramanmaras, Turkey earthquake sequence from InSAR and optical data. *Geophysical Research Letters*, *50*(17), e2023GL104693. https://doi.org/10.1029/2023gl104693

Institut de physique du globe de Paris (IPGP), and École et Observatoire des Sciences de la Terre de Strasbourg (EOST). (1982). *GEOSCOPE, French Global Network of broad band seismic stations*. Institut de physique du globe de Paris (IPGP), Université de Paris. https://doi.org/10.18715/GEOSCOPE

Institute of Earth Sciences, Academia Sinica, Taiwan. (1996). Broadband array in Taiwan for Seismology. *International Federation of Digital Seismograph Networks*. [Dataset]. https://doi.org/10.7914/SN/TW

Ishii, M., Shearer, P. M., Houston, H., & Vidale, J. E. (2005). Extent, duration and speed of the 2004 Sumatra-Andaman earthquake imaged by the Hi-Net array. *Nature*, *435*(7044), 933–936. https://doi.org/10.1038/nature03675

Ji, C., Wald, D. J., & Helmberger, D. V. (2002). Source description of the 1999 Hector Mine, California, earthquake, part I: Wavelet domain inversion theory and resolution analysis. *Bulletin of the Seismological Society of America*, *92*(4), 1192–1207.

Jia, Z., Jin, Z., Marchandon, M., Ulrich, T., Gabriel, A.-A., Fan, W., et al. (2023). The complex dynamics of the 2023 Kahramanmaraş, Turkey, M w 7.8-7.7 earthquake doublet. *Science*, eadi0685.

Kanamori, H., Anderson, D. L., & Heaton, T. H. (1998). Frictional melting during the rupture of the 1994 Bolivian earthquake. *Science*, *279*(5352), 839–842. https://doi.org/10.1126/science.279.5352.839

Kanamori, H., & Brodsky, E. E. (2004). The physics of earthquakes. *Reports on Progress in Physics*, *67*(8), 1429–1496. https://doi.org/10.1088/0034-4885/67/8/r03

Kyrgyz Institute of Seismology, K. I. S. (2007). Kyrgyz digital network. *International Federation of Digital Seismograph Networks*. [Dataset]. https://doi.org/10.7914/SN/KR

Lambert, V., Lapusta, N., & Perry, S. (2021). Propagation of large earthquakes as self-healing pulses or mild cracks. *Nature*, *591*(7849), 252–258. https://doi.org/10.1038/s41586-021-03248-1

Lay, T., Kanamori, H., Ammon, C. J., Koper, K. D., Hutko, A. R., Ye, L., et al. (2012). Depth-varying rupture properties of subduction zone megathrust faults. *Journal of Geophysical Research*, *117*(B4). https://doi.org/10.1029/2011jb009133

Li, B., Wu, B., Bao, H., Oglesby, D. D., Ghosh, A., Gabriel, A. A., et al. (2022). Rupture heterogeneity and directivity effects in back-projection analysis. *Journal of Geophysical Research: Solid Earth*, *127*(3), e2021JB022663. https://doi.org/10.1029/2021jb022663

Liu, C., Lay, T., Wang, R., Taymaz, T., Xie, Z., Xiong, X., et al. (2023). Complex multi-fault rupture and triggering during the 2023 earthquake doublet in southeastern Türkiye. *Nature Communications*, *14*(1), 5564. https://doi.org/10.1038/s41467-023-41404-5

Lomax, A. (2023). Precise, NLL-SSST-coherence hypocenter catalog for the 2023 Mw 7.8 and Mw 7.6 SE Turkey earthquake sequence.

Ma, Z., Li, C., Jiang, Y., Chen, Y., Yin, X., Aoki, Y., et al. (2024). Space geodetic insights to the dramatic stress rotation induced by the February 2023 Turkey-Syria earthquake doublet. *Geophysical Research Letters*, *51*(6), e2023GL107788. https://doi.org/10.1029/2023gl107788

Ma, Z., Zeng, H., Luo, H., Liu, Z., Jiang, Y., Aoki, Y., et al. (2024). Slow rupture in a fluid-rich fault zone initiated the 2024 M w 7.5 Noto earthquake. *Science*, *385*(6711), 866–871. https://doi.org/10.1126/science.ado5143

Madariaga, R. (1983). High frequency radiation from dynamic earthquake. *Annals of Geophysics*, *1*, 17.

Mai, P. M., Aspiotis, T., Aquib, T. A., Cano, E. V., Castro-Cruz, D., Espindola-Carmona, A., et al. (2023). The destructive earthquake doublet of 6 february 2023 in south-central Türkiye and northwestern Syria: Initial observations and analyses. *The Seismic Record*, *3*(2), 105–115. https://doi.org/10.1785/0320230007

Melgar, D., Taymaz, T., Ganas, A., Crowell, B. W., Öcalan, T., Kahraman, M., et al. (2023). Sub-and super-shear ruptures during the 2023 Mw 7.8 and Mw 7.6 earthquake doublet in SE Türkiye. *Seismica*, *2*(3). https://doi.org/10.26443/seismica.v2i3.387

Meng, L. S., Inbal, A., & Ampuero, J.-P. (2011). A window into the complexity of the dynamic rupture of the 2011 Mw 9 Tohoku-Oki earthquake. *Geophysical Research Letters*, *38*(7). https://doi.org/10.1029/2011gl048118

Nalbant, S. S., McCloskey, J., Steacy, S., & Barka, A. A. (2002). Stress accumulation and increased seismic risk in eastern Turkey. *Earth and Planetary Science Letters*, *195*(3–4), 291–298. https://doi.org/10.1016/s0012-821x(01)00592-1

Natural Resources Canada. (1975). Canadian national seismograph network. *Natural Resources Canada*. [Dataset]. https://doi.org/10.7914/SN/CN

Noda, H., & Lapusta, N. (2013). Stable creeping fault segments can become destructive as a result of dynamic weakening. *Nature*, *493*(7433), 518–521. https://doi.org/10.1038/nature11703

Ogden, C., & Bastow, I. (2022). The crustal structure of the Anatolian Plate from receiver functions and implications for the uplift of the central and eastern Anatolian plateaus. *Geophysical Journal International*, *229*(2), 1041–1062. https://doi.org/10.1093/gji/ggab513

Okuwaki, R., Yagi, Y., Taymaz, T., & Hicks, S. P. (2023). Multi-scale rupture growth with alternating directions in a complex fault network during the 2023 south-eastern Türkiye and Syria earthquake doublet. *Geophysical Research Letters*, *50*(12), e2023GL103480. https://doi.org/10.1029/2023gl103480

Ranjith, K., & Rice, J. (2001). Slip dynamics at an interface between dissimilar materials. *Journal of the Mechanics and Physics of Solids*, *49*(2), 341–361. https://doi.org/10.1016/s0022-5096(00)00029-6

Regional Integrated Multi-Hazard Early Warning System (RIMES Thailand). (2008). Regional integrated multi-hazard early warning system. *International Federation of Digital Seismograph Networks*. [Dataset]. https://doi.org/10.7914/SN/RM

Reitman, N. G., Briggs, R. W., Barnhart, W. D., Hatem, A. E., Thompson Jobe, J. A., DuRoss, C. B., et al. (2023). Rapid surface rupture mapping from satellite data: The 2023 Kahramanmaraş, Turkey (Türkiye), earthquake sequence. *The Seismic Record*, *3*(4), 289–298. https://doi.org/10.1785/0320230029

Ren, C., Wang, Z., Taymaz, T., Hu, N., Luo, H., Zhao, Z., et al. (2024). Supershear triggering and cascading fault ruptures of the 2023 Kahramanmaraş, Türkiye, earthquake doublet. *Science*, *383*(6680), 305–311. https://doi.org/10.1126/science.adi1519

Rodgers, A. J., Krischer, L., Afanasiev, M., Boehm, C., Doody, C., & Simmons, N. (2024). Adjoint waveform tomography for crustal and upper mantle structure of the Middle East and southwest Asia for improved waveform simulations using openly available broadband data. *Bulletin of the Seismological Society of America*, *114*(3), 1365–1391. https://doi.org/10.1785/0120230248

Rosakis, A., Abdelmeguid, M., & Elbanna, A. (2023). Evidence of early supershear transition in the Mw 7.8 Kahramanmara\c {s} earthquake from near-field records. *arXiv preprint arXiv:2302.07214*.

Rosakis, A. J., Xia, K., Lykotrafitis, G., & Kanamori, H. (2007). 4.08 - dynamic shear rupture in frictional interfaces: Speeds, directionality, and modes. In G. Schubert (Ed.), *Treatise on geophysics* (2nd ed., pp. 183–213). Elsevier. https://doi.org/10.1016/B978-0-444-53802-4.00072-5

Sammis, C. G., Rosakis, A. J., & Bhat, H. S. (2010). Effects of off-fault damage on earthquake rupture propagation: Experimental studies. *Mechanics, structure and evolution of fault zones*, 1629–1648. https://doi.org/10.1007/978-3-0346-0138-2_5

Scripps Institution of Oceanography. (1986). Global seismograph network - IRIS/IDA. *International Federation of Digital Seismograph Networks*. [Dataset]. https://doi.org/10.7914/SN/II

Shlomai, H., & Fineberg, J. (2016). The structure of slip-pulses and supershear ruptures driving slip in bimaterial friction. *Nature Communications*, *7*(1), 11787. https://doi.org/10.1038/ncomms11787

Styron, R., & Pagani, M. (2020). The GEM global active faults database. *Earthquake Spectra*, *36*(1_suppl), 160–180. https://doi.org/10.1177/8755293020944182

Toda, S., Stein, R., Özbakir, A., Gonzalez-Huizar, H., Sevilgen, V., Lotto, G., & Sevilgen, S. (2023). Stress change calculations provide clues to aftershocks in 2023 Türkiye earthquakes. *Temblor*.

Uchide, T., Yao, H., & Shearer, P. M. (2013). Spatio-temporal distribution of fault slip and high-frequency radiation of the 2010 El Mayor-Cucapah, Mexico earthquake. *Journal of Geophysical Research: Solid Earth*, *118*(4), 1546–1555. https://doi.org/10.1002/jgrb.50144

Voelker, B., Milillo, P., Tavakkoliestahbanati, A., Macchiarulo, V., Giardina, G., Recla, M., et al. (2024). *The EEFIT remote sensing reconnaissance mission for the February 2023 Turkey earthquakes*. Ieee J-Stars.

Wang, Z., Zhang, W., Taymaz, T., He, Z., Xu, T., & Zhang, Z. (2023). Dynamic rupture process of the 2023 Mw 7.8 Kahramanmaraş earthquake (SE Türkiye): Variable rupture speed and implications for seismic hazard. *Geophysical Research Letters*, *50*(15), e2023GL104787. https://doi.org/10.1029/2023gl104787

Weertman, J. (1980). Unstable slippage across a fault that separates elastic media of different elastic constants. *Journal of Geophysical Research*, *85*(B3), 1455–1461. https://doi.org/10.1029/jb085ib03p01455

Wei, S., Fielding, E., Leprince, S., Sladen, A., Avouac, J. P., Helmberger, D., et al. (2011). Superficial simplicity of the 2010 El Mayor-Cucapah earthquake of Baja California in Mexico. *Nature Geoscience*, *4*(9), 615–618. https://doi.org/10.1038/ngeo1213

Wei, S., Graves, R., Helmberger, D., Avouac, J.-P., & Jiang, J. (2012). Sources of shaking and flooding during the Tohoku-Oki earthquake: A mixture of rupture styles. *Earth and Planetary Science Letters*, *333*, 91–100. https://doi.org/10.1016/j.epsl.2012.04.006

Wei, S., Zeng, H., Shi, Q., Liu, J., Luo, H., Hu, W., et al. (2022). Simultaneous rupture propagation through fault bifurcation of the 2021 Mw7. 4 Maduo earthquake. *Geophysical Research Letters*, *49*(21), e2022GL100283. https://doi.org/10.1029/2022gl100283

Xia, K., Rosakis, A. J., & Kanamori, H. (2004). Laboratory earthquakes: The sub-Rayleigh-to-supershear rupture transition. *Science*, *303*(5665), 1859–1861. https://doi.org/10.1126/science.1094022

Xia, K., Rosakis, A. J., Kanamori, H., & Rice, J. R. (2005). Laboratory earthquakes along inhomogeneous faults: Directionality and supershear. *Science*, *308*(5722), 681–684. https://doi.org/10.1126/science.1108193

Xu, L., Mohanna, S., Meng, L., Ji, C., Ampuero, J.-P., Yunjun, Z., et al. (2023). The overall-subshear and multi-segment rupture of the 2023 Mw7. 8 Kahramanmaraş, Turkey earthquake in millennia supercycle. *Communications Earth and Environment*, *4*(1), 379. https://doi.org/10.1038/s43247-023-01030-x

Yao, H., Gerstoft, P., Shearer, P. M., & Mecklenbräuker, C. (2011). Compressive sensing of the Tohoku-Oki Mw 9.0 earthquake: Frequency-dependent rupture modes. *Geophysical Research Letters*, *38*(20). https://doi.org/10.1029/2011gl049223

Yu, X., Hu, X., Song, Y., Xu, S., Li, X., Song, X., et al. (2024). Intelligent assessment of building damage of 2023 Turkey-Syria Earthquake by multiple remote sensing approaches. *npj Natural Hazards*, *1*(1), 3. https://doi.org/10.1038/s44304-024-00003-0

Zeng, H., Wei, S., & Rosakis, A. (2022). A travel-time path calibration strategy for back-projection of large earthquakes and its application and validation through the segmented super-shear rupture imaging of the 2002 Mw 7.9 Denali earthquake. *Journal of Geophysical Research: Solid Earth*, *127*(6), e2022JB024359. https://doi.org/10.1029/2022jb024359

Zhang, Y., Tang, X., Liu, D., Taymaz, T., Eken, T., Guo, R., et al. (2023). Geometric controls on cascading rupture of the 2023 Kahramanmaraş earthquake doublet. *Nature Geoscience*, *16*(11), 1–7. https://doi.org/10.1038/s41561-023-01283-3

Zhu, L. P., & Rivera, L. A. (2002). A note on the dynamic and static displacements from a point source in multilayered media. *Geophysical Journal International*, *148*(3), 619–627. https://doi.org/10.1046/j.1365-246x.2002.01610.x

Zhu, W. M., Zhao, L. F., Xie, X. B., He, X., Zhang, L., & Yao, Z. X. (2023). High-resolution broadband Lg attenuation structure of the Anatolian crust and its implications for mantle upwelling and plateau uplift. *Geophysical Research Letters*, *50*(6), e2023GL103470. https://doi.org/10.1029/2023gl103470